RSC Advances

ROYAL SOCIETY OF CHEMISTRY

www.rsc.org/advances

MnO nanoparticles embedded in carbon matrix for high performance Li ion battery anode

Chunyu Zhu [a]*, Nan Sheng [a], Tomohiro Akiyama [a]

[a]Center for Advanced Research of Energy & Materials, Hokkaido University, Sapporo 060-8628, Japan

*Corresponding author: Tel.: +81-11-706-6842; Fax: +81-11-726-0731.
E-mail address: chunyu6zhu@gmail.com or chunyu6zhu@eng.hokudai.ac.jp (Chunyu Zhu).

Abstract

Manganese oxides are promising anode materials for lithium ion batteries based on conversion reactions. In this paper, MnO nanoparticles that were embedded in a carbon matrix were directly produced by a facile glycine-nitrate-based solution combustion synthesis (SCS) process with subsequent calcination treatment under inert atmosphere. The effect of the amount of glycine used in the SCS process and the calcination temperature on the composite products as well as their electrochemical properties were investigated. The carbon content in the composite can be controlled by changing the amount of glycine, while the crystallinity, morphology of the MnO particles, phase composition, and the characteristics of the carbon materials were quite dependent on the calcination temperature. The sample calcined at 700 ^{o}C with a composite carbon content of around 27.7% provided the best electrochemical performance. This sample delivered a reversible specific capacity of 437.6 mAh g^{-1} at a high current density of 500 mA g^{-1} after 300 cycles. The enhanced electrochemical properties can be ascribed to the formation of a MnO nanoparticle/carbon composite. The carbon matrix offered a connected structure for fast Li ion and electron transportation, and worked as a buffer to accommodate the volume change upon lithium insertion/extraction.

Keywords: manganese oxide, lithium ion battery, anode material, composite, solution combustion synthesis

Introduction

Over the past few decades, lithium ion batteries (LIBs) have attracted attention as ideal power sources for mobile electronic devices and electric vehicles. However, conventional graphite anodes used in commercialized LIBs cannot meet the increasing demands for large energy and power density, because of their limited theoretical capacity of 372 mAh g^{-1}.[1, 2] Various candidates, such as silicon,[3-7] tin,[8-12] and transition metal oxides (TMOs)[13-18], have been widely investigated for next-generation anode materials. Among the TMOs, MnO has been recognized as one of the most promising materials for LIB anodes, because of its low conversion potential, low potential hysteresis (<0.8 V), high theoretical capacity (755 mAh g^{-1}), low cost, and environmental benignity.[19] However, the practical application of MnO has been hindered by many obstacles, including poor durability and low rate capability. These are mainly caused by the low electrical conductivity and huge volume change during Li^+ intercalation-deintercalation via the conversion reaction ($MnO + 2Li^+ + 2e^- = Mn + Li_2O$). During cycling, the repeated expansion and shrinkage in volume lead to the pulverization of the MnO electrode, which results in rapid performance degradation. Furthermore, the low electrical conductivity of MnO electrodes usually results in inferior rate capability.[20-23] To date, a number of efforts have been devoted to solve the above problems. An effective strategy is to synthesize nanosized MnO to shorten the diffusion path for lithium ions and electrons.[24, 25] Another approach is to produce a composite by hybridizing the MnO nanostructure with a carbonaceous material, which acts as both a volume buffer and a conductive network.[22, 26-28] Nevertheless, it remains a great challenge to fabricate MnO/C anodes by a facile and scalable method.

Glycine-nitrate-based solution combustion synthesis (SCS) is a highly exothermic and self-sustaining reaction process, which is performed by heating a solution mixture of aqueous metal nitrates and fuels of glycine. This approach has been used to synthesize a variety of functional oxides, such as perovskite catalysts[29, 30], and cathode materials for LIBs[31, 32]. This method offers several benefits, such as (1) the utilization of an exothermic reaction requiring no additional energy during the combustion process, (2) larger surface areas of nanosized or porous products, (3) homogeneous doping of trace amounts of various elements in a single step. By controlling the combustion reaction conditions to avoid the complete combustion of

the carbonaceous material, the remaining carbon material and metal oxides can form composites for advanced LIB anode materials. This can be achieved by (1) adding excess amount of fuel and (2) lowering the combustion temperature to avoid the combustion of carbon.

In this study, we report the facile synthesis of a MnO/C composite via glycine-nitrate-based solution combustion synthesis, by controlling the amount of glycine and the subsequent calcination conditions. The resulting composites exhibited enhanced cycling and rate performance for the anodes of LIBs, as a consequence of the synergetic effects between the carbon matrix and MnO nanocrystals.

Experimental section

Solution combustion synthesis of MnO/C composite: Solution combustion synthesis proceeded by using the gels of manganese nitrate ($Mn(NO_3)_2$, 10 mmol) and glycine (NH_2CH_2COOH) with distilled water as a solvent in molar ratios of 1:3 (sample n3) and 1:4 (sample n4). The combustion process was conducted in a lab-made apparatus, as described in previous studies, [29-33] by heating the gels up to 300 ^oC under air. After SCS, the obtained black samples were milled in a mortar-pestle and subsequently heat-treated under Ar flow at temperatures of 600, 700, or 800 ^oC for 2 h. In total, four samples were produced, which were named n3-Ar 600 ^oC-2h, n4-Ar 600 ^oC-2h, n4-Ar 700 ^oC-2h, and n4-Ar 800 ^oC-2h.

Material characterization: The as-prepared products were characterized by powder X-ray diffraction (XRD, Rigaku Miniflex, CuKα), transmission electron microscopy (TEM, 200 kV, JEM-2010F), and scanning electron microscopy (SEM, JEOL, JSM-7400F) combined with X-ray energy dispersive spectrometry (EDS) to determine their crystalline structure, morphology and elemental composition. A thermogravimetric (TG, Mettler Toledo) analyzer combined with a mass spectrometer (MS) was used to determine the reaction behavior of the SCSed precursor during heat treatment and the carbon content of the composites. Raman spectra of the samples were acquired from a RENISHAW Raman spectrometer using an excitation wavelength of 532 nm.

Electrochemical measurements: Electrochemical tests were performed using a two-electrode union-joint cell of the modified Swagelok design. An assembled cell contained a lithium disk as a counter/reference electrode and a working electrode. The working electrode consisted of the active material, conductive carbon (acetylene black), and polyvinylidene fluoride (PVDF) binder in a weight ratio of 80:10:10, which were pasted onto a Cu foil current collector by using N-methylpyrrolidone (NMP) as solvent. The cell was assembled in an Ar-filled glove-box. A 1 M solution of $LiPF_6$ dissolved in a 50:50 (v/v) mixture of ethylene carbonate (EC) and dimethyl carbonate (DMC) was used as the electrolyte, with a Celgard glass fiber as the separator. Galvanostatic discharge/charge measurements were performed using a battery tester (KIKUSUI, PFX2011) in a potential range of 3.0 and 0.01 V versus Li/Li^+ at a constant temperature of 25 ºC. Cyclic voltammetry

(CV) analysis was carried out using a potentiostat/galvanostat apparatus (Autolab, PGSTAT128N) at a potential scanning rate of 0.1 mV s^{-1} in a voltage range of 3.0-0.0 V.

Results and discussion

Figure 1 shows the XRD patterns of the samples obtained at different stages of treatment. After the SCS process, the n3 sample consisted of a Mn_3O_4 phase (JCPD card 80-0382), while the n4 sample had an amorphous pattern. The sample of n3-Ar 600 ^oC-2h presented a mixture of MnO (JCPD card 07-0230) and Mn_3O_4. After heat-treatment at 600 ^oC, 700 ^oC and 800 ^oC for 2 h under Ar flow, the n4-Ar 600 ^oC-2h sample retained an amorphous pattern, while the n4-Ar 700 ^oC-2h sample presented the peaks indicative of cubic MnO, and the n4-Ar 800 ^oC-2h sample showed a main phase of MnO with a small peak at 42^o which can be indexed to metallic β-Mn (JCPD card 24-0734). For the n3 sample, the manganese nitrate-glycine gel presented a relatively complete combustion reaction between the nitrate oxidant and glycine fuel and only a small amount of carbon was left in the sample, however, with the addition of sufficient glycine as the carbon source, the n4 sample included enough carbon in the products.

Figure 2 shows the Raman spectra of the four calcined samples. Two minor peaks at 319, 375 cm^{-1} and a dominant peak at 652 cm^{-1} were observed in the Raman scattering spectra for the sample of n3-Ar 600 ^oC-2h, which were consistent with the reported E_g, T_{2g} and A_{1g} active modes of Mn_3O_4.[34, 35] Here, in the raman spectra, the typical peaks of Mn_3O_4 rather than MnO were observed for the bare oxides sample, although the dominant phase of the oxides was MnO as confirmed by XRD analysis. This is because of that MnO is easily transformed into Mn_3O_4 by the local heating effect and photochemically induced transformations when the beam intensity is more than 1.1 MW during the Raman measurements.[36, 37] The typical Mn_3O_4 raman scattering peak at about 652 cm^{-1} was also observed for the MnO/C composite samples. Two peaks at about 1357 and 1573 cm^{-1} that can be assigned to the D and G bands of carbon were observed for the samples of n4-Ar 600 ^oC-2h, n4-Ar 700 ^oC-2h, and n4-Ar 700 ^oC-2h. The 1357 cm^{-1} band corresponds to the A_{1g} vibration mode of the disordered carbon (D-bond) and the 1573 cm^{-1} band is related to the E_{2g} vibration mode of the ordered graphitic carbon (G-bond). The ratios of the intensities of the D-band and the G-band, I_D/I_G, for the MnO/C composite materials are larger than 1. These values are greatly higher than that of the fully graphitized carbon, indicating a high defective state of the carbon matrix. This defective structure may be favourable for enhancing the ionic conductivity of the electrolyte.[38, 39] In fact,

the carbon matrix of the composite materials are N-containing carbons, as confirmed in the following MS and EDS measurement.

The thermal behavior of the SCSed precursors and the carbon contents of the final products were evaluated by TG analysis. As shown in Figure 3-(a), the SCSed precursors were heated under Ar flow at a temperature ramp of 10 ^{o}C min^{-1}. The n3 sample lost about 12% of its weight in the temperatrue range of around 400–700 ^{o}C, which corresponded to the partial reduction of Mn_3O_4 to MnO by the limited amount of carbon that remained in this sample. The precursor of n4 experienced a sharp weight loss at 150–300 ^{o}C due to decomposition of the remaining glycine and nitrate. After that, the pyrolyzed precursor showed a slow but continous weight loss until 830 ^{o}C, due to the decomposition of the unstable carbonaceous materials and the carbon reduction of MnO_x ($x > 1$) to MnO. A small steep weight loss at 830 to 880 ^{o}C indicated the reduction of MnO to metallic Mn. The carbon contents of composites were calculated by the TG weight loss by air-combustion of the samples, as shown in Figure 3-(b). For the samples obtained from the n4 precursor, the weight changes at 250–500 ^{o}C corresponded to the reaction of $MnO/C + O_2 \rightarrow Mn_2O_3 + CO_2$. MnO was oxidized to Mn_2O_3 introducing a weight increase, while carbon was oxidized to CO_2 gas resulting in a weight loss. The carbon contents for samples of n4-Ar 600 ^{o}C-2h, n4-Ar 700 ^{o}C-2h, and n4-Ar 800 ^{o}C-2h were calcualted to be 27.7%, 24.1%, and 19.7%, respectively. However, upon heating the sample of n3-Ar 600 ^{o}C-2h, the weight increased between 250–500 ^{o}C was due to oxidiation of MnO and Mn_3O_4 to Mn_2O_3. Gas analysis using MS indicated that CO_2 and NO were formed during the TG air-combustion of n4-Ar 600 ^{o}C-2h and n4-Ar 700 ^{o}C-2h, while no obvious NO peak was detected for the sample of n4-Ar 800 ^{o}C-2h. These results pointed to the N-doping of carbon for the samples treated at 600 and 700 ^{o}C, which was further confirmed by EDS elemental analysis in the following paragraph. It has been reported that N-doping can enhance the electronic conductivity of carbon-based materials, therefore improving the electrochemical performance. Furthermore, this kind of N-doped carbon possesses more Li storage sites than graphitic carbon, increasing its capacity.[38-40]

Figure 4 shows the typical SEM images at different magnifications for the MnO/C composites or MnO_x products. The product of n3-Ar 600 ^{o}C-2h showed nanoparticles of

around 50–300 nm in size. The samples of MnO/C composites treated at different temperatures (n4-Ar 600 ^{o}C-2h, n4-Ar 700 ^{o}C-2h, and n4-Ar 800 ^{o}C-2h) presented micron-sized irregular bulk shapes ranging from several microns to 40–50 microns. The bulk shapes contained some macropores of several hundreds of nanometers in size. The surfaces of the these bulk materials were very smooth and were not conductive to large surface area. Furthermore, it is very interesting to find some cubic nanoparticles that are inserted on the surface of the bulks for the samples of n4-Ar 700 ^{o}C-2h and n4-Ar 800 ^{o}C-2h. The cubic particles showed sizes of around 200–400 nm. These cubic particles were confirmed to be MnO by the EDS elemental mapping (Figure 5), which showed the accumulation of manganese and oxygen elements in the cubic shapes. The EDS spectra of the MnO/C composites indicated the existence of Mn, O, and C. N was also detected in the samples of n4-Ar 600 ^{o}C-2h and n4-Ar 700 ^{o}C-2h, while the spectrum of n4-Ar 800 ^{o}C-2h did not have an N. This is consistent with the results from analyzing of the combustion gases using MS as showing Figure 3.

Figure 6 displays the discharge-charge cycling performance of the electrodes at 0.5 A g^{-1} and a stepwise increase of the current rate to 2.0 A g^{-1} in the range of 3.0–0.01 V vs. Li. It can be clearly observed that the samples of n4-Ar 600 ^{o}C-2h and n4-Ar 700 ^{o}C-2h illustrated superior cycling performance compared to the samples of n4-Ar 800 ^{o}C-2h and n3-Ar 600 ^{o}C-2h. The discharge capacity of n3-Ar 600 ^{o}C-2h (a bare mixture of MnO and Mn_3O_4) decreased upon cycling from 1035.7 mAh g^{-1} at the first cycle to 545.3 mAh g^{-1} at the second cycle and 141.7 mAh g^{-1} after 190 cycles at a constant current rate of 0.5 A g^{-1}. The sample of n4-Ar 800 ^{o}C-2h indicated an initial discharge capacity of 520.3 mAh g^{-1} and a greatly decreased capacity of 274.4 mAh g^{-1} at the second cycle, after which the discharge capacity slowly decreased and then stabalized at around 250 mAh g^{-1} after 200 cycles, at a constant current rate of 0.5 A g^{-1}. Samples of n4-Ar 600 ^{o}C-2h and n4-Ar 700 ^{o}C-2h were first cycled at 0.5 A g^{-1} for 120 cycles, then the current rates were increased stepwise to 0.7 A g^{-1}, 1.0 A g^{-1}, 1.5 A g^{-1}, 2.0 A g^{-1}, and finally backed to 0.5 A g^{-1}. In the first 120 cycles at 0.5 A g^{-1}, sample n4-Ar 700 ^{o}C-2h showed an initial discharge capacity of 770.5 mAh g^{-1} which subsequently stablized at around 500 mAh g^{-1}, while sample n4-Ar 600 ^{o}C-2h presented an initial discharge capacity of 826.0 mAh g^{-1} which decreased gradually from 540.7 mAh g^{-1} at

the second cycle to 440.5 mAh g^{-1} at the 21st cycle, after which the discharge capacity slowly increased to around 480.0 mAh g^{-1} at the 120th cycle. At current rates of 0.7, 1.0, 1.5, and 2.0 A g^{-1}, the sample of n4-Ar 700 ^{o}C-2h showed reversible capacities of 443.8, 385.1, 309.2, and 248.5 mAh g^{-1}, respectively, while the capacities of sample n4-Ar 600 ^{o}C-2h were 433.7, 372.2, 290.3, and 224.8 mAh g^{-1}, respectively. The current rate was finally backed to 0.5 A g^{-1} and the samples were cycled to 300 cycles, showing final discharge capacities of 437.6 and 397.2 mAh g^{-1} for n4-Ar 700 ^{o}C-2h and n4-Ar 600 ^{o}C-2h, respectively. Figure 6 also presents the coulombic efficiency of lithium deintercalation/intercalation vs. cycling number, and the results indicate an efficiency sequence of n4-Ar 700 ^{o}C-2h > n4-Ar 600 ^{o}C-2h > n4-Ar 800 ^{o}C-2h > n3-Ar 600 ^{o}C-2h. The coulombic efficiency for n4-Ar 700 ^{o}C-2h steadily reached and stablized at > 99% from the 6th cycle.

Figure 7 presents the discharge-charge voltage profiles of the electrodes at different cycles. For the sample of n3-Ar 600 ^{o}C-2h, which was a mixture of Mn_3O_4 and MnO, the first discharge curve showed a sloping voltage from 1.2 to 0.3 V, which might originate from the formation of a solid–electrolyte interface (SEI) film on the electrode surface due to decomposition of the electrolyte solution.[15, 24] The voltage plateau at around 0.3–0.15 V related to the reduction of Mn_3O_4 to MnO, and the long plateau below 0.15 V represented the reduction of Mn^{2+} to Mn^0. For the initial charge curve, the electrode showed a slope in the voltage range between 1.0 and 1.5 V, which was related to the oxidation of Mn to MnO/Mn_3O_4. For the other three carbon composited MnO/C electrodes, in their first discharge profiles, all the samples presented a short steep voltage drop ranging from 1.5 to 0.7 V, as derived from the formation of an SEI film. In the voltage range below 0.7 V, the electrodes showed a continuous potential decrease until 0.01 V and no obvious voltage plateau could be found, which might be caused by the large amount of compositing carbon. The potential drops from 0.7 V to 0.01 V represented the reduction of MnO to Mn and the Li storage in the carbon material. In the opposite charge process, the profiles showed gentle slopes and not an obvious potential plateau could be found, as compared with the bare MnO_x electrode. The typical discharge-charge profiles at different current rates for the sample of n4-Ar 700 ^{o}C-2h are shown in Figure 7 (e). As the current rate increases, the electrodes showed decreased capacities due to the increased polarization effect.

The lithium ion storage properites of the samples were also examined by CV measurements. Figure 8 shows the typical CV curves in the first three cycles, which were scanned at a rate of 0.1 mV s^{-1} in the potential range between 3.0 and 0.0 V. In the first cathodic process for n3-Ar 600 ^{o}C-2h sample, the two intense peaks at low potential were attributed to the reduction of Mn_3O_4 to MnO, and the further reduction of MnO to Mn. This is consistent with that of the first discharge voltage profile showing two voltage plateaus at low potential. In the following anodic sweep, one broad peak located at around 1.3 V was observed, indicating the reversible oxidation of Mn to manganese oxides (MnO/Mn_3O_4). In the second cathodic process, this sample showed two seperate peaks at around 0.55 V and 0.02 V; however, in the third cathodic process, the sample presented a broad peak at < 0.6 V. In the second and third anodic sweeps, broad peaks at around 1.3–1.4 V were observed. The CV profiles of MnO/C composites were quite different from that of the bare MnO_x electrode. In the cathodic process, all composite electrodes presented two typical peaks at around 0.25–0.5 V and 0.02 V. The broad peaks at around 0.25–0.5 V represented the reduction of MnO to Mn, while the sharp peaks at around 0.02 V indicated the Li ion storage by the composite carbon. The anodic sweeps showed broad peaks at around 1.1 V, indicating the reversible oxidation of Mn to manganese oxide. The covered CV areas indicated the Li storage capacity of the as-prepared electrode, and it is obvious to see that the capacity of sample n4-Ar 800 ^{o}C-2h was less than that of n4-Ar 700 ^{o}C-2h and n4-Ar 600 ^{o}C-2h, which was also confirmed by the galvanostatic cycling measurements. Furthermore, the cathodic and anodic reaction hystereses were shortened for the composite electrode as compared with the bare MnO_x electrode, illustrating higher coulombic efficiencies for the composite materials.

Conclusions

In summary, MnO/carbon composites were produced by a facile glycine-nitrate-based solution combustion synthesis process, following by a calcination treatment under inert atmosphere. The carbon content of the composites and its characteristics were controlled by the amount of glycine and the calcination temperature, which influenced the electrochemical performance. The MnO/C composite with a carbon content of 27.7% , which was calcined at 700 ^{o}C, exhibited the best electrochemical properties including cycling and rate performance. The capacity of this sample reached 437.6 mAh g^{-1} at a high current density of 500 mA g^{-1} after 300 cycles. The synthetic strategy is low cost and offers easy production, which can be extended to prepare other carbon-composited materials for a variety of applications.

References

1. W. W. Lee and J.-M. Lee, *Journal of Materials Chemistry A*, 2014, 2, 1589-1626.
2. S. Goriparti, E. Miele, F. De Angelis, E. Di Fabrizio, R. Proietti Zaccaria and C. Capiglia, *Journal of Power Sources*, 2014, 257, 421-443.
3. Y. Zhou, X. Jiang, L. Chen, J. Yue, H. Xu, J. Yang and Y. Qian, *Electrochimica Acta*, 2014, 127, 252-258.
4. T. Yim, S. J. Choi, Y. N. Jo, T.-H. Kim, K. J. Kim, G. Jeong and Y.-J. Kim, *Electrochimica Acta*, 2014, 136, 112-120.
5. Z.-L. Xu, B. Zhang, Z.-Q. Zhou, S. Abouali, M. Akbari Garakani, J. Huang, J.-Q. Huang and J.-K. Kim, *RSC Advances*, 2014, 4, 22359-22366.
6. Y. Xu, Y. Zhu and C. Wang, *Journal of Materials Chemistry A*, 2014, 2, 9751-9757.
7. D. P. Wong, R. Suriyaprabha, R. Yuvakumar, V. Rajendran, Y.-T. Chen, B.-J. Hwang, L.-C. Chen and K.-H. Chen, *Journal of Materials Chemistry A*, 2014, 2, 13437-13441.
8. C.-j. Liu, F.-h. Xue, H. Huang, X.-h. Yu, C.-j. Xie, M.-s. Shi, G.-z. Cao, Y.-g. Jung and X.-l. Dong, *Electrochimica Acta*, 2014, 129, 93-99.
9. N. Li, H. Song, H. Cui, G. Yang and C. Wang, *Journal of Materials Chemistry A*, 2014, 2, 2526-2537.
10. M. Ara, K. Wadumesthrige, T. Meng, S. O. Salley and K. Y. S. Ng, *RSC Advances*, 2014, 4, 20540-20547.
11. Z. Tan, Z. Sun, H. Wang, Q. Guo and D. Su, *Journal of Materials Chemistry A*, 2013, 1, 9462-9468.
12. G. Saito, C. Zhu and T. Akiyama, *Advanced Powder Technology*, 2014, 25, 728-732.
13. M. V. Reddy, G. V. Subba Rao and B. V. R. Chowdari, *Chemical Reviews*, 2013, 113, 5364-5457.
14. P. Lian, J. Wang, D. Cai, L. Ding, Q. Jia and H. Wang, *Electrochimica Acta*, 2014, 116, 103-110.
15. Z. Bai, N. Fan, Z. Ju, C. Guo, Y. Qian, B. Tang and S. Xiong, *Journal of Materials Chemistry A*, 2013, 1, 10985-10990.
16. L. Zhuo, Y. Wu, J. Ming, L. Wang, Y. Yu, X. Zhang and F. Zhao, *Journal of Materials Chemistry A*, 2013, 1, 1141-1147.
17. X. Zhang, H. Liu, S. Petnikota, S. Ramakrishna and H. J. Fan, *Journal of Materials Chemistry A*, 2014, 2, 10835-10841.
18. W. Zhang, H. Wang, Y. Zhang, Z. Yang, Q. Wang, J. Xia and X. Yang, *Electrochimica Acta*, 2013, 113, 63-68.
19. Y. Deng, L. Wan, Y. Xie, X. Qin and G. Chen, *RSC Advances*, 2014, 4, 23914-23935.
20. T. Wang, Z. Peng, Y. Wang, J. Tang and G. Zheng, *Sci. Rep.*, 2013, 3.
21. L. Su, Y. Zhong, J. Wei and Z. Zhou, *RSC Advances*, 2013, 3, 9035-9041.
22. W. Luo, X. Hu, Y. Sun and Y. Huang, *ACS Applied Materials & Interfaces*, 2013, 5, 1997-2003.
23. X. Zhang, Z. Xing, L. Wang, Y. Zhu, Q. Li, J. Liang, Y. Yu, T. Huang, K. Tang, Y. Qian and X. Shen, *Journal of Materials Chemistry*, 2012, 22, 17864-17869.
24. X. Li, D. Li, L. Qiao, X. Wang, X. Sun, P. Wang and D. He, *Journal of Materials Chemistry*, 2012, 22, 9189-9194.
25. G.-L. Xu, Y.-F. Xu, J.-C. Fang, F. Fu, H. Sun, L. Huang, S. Yang and S.-G. Sun, *ACS Applied Materials & Interfaces*, 2013, 5, 6316-6323.
26. S. Guo, G. Lu, S. Qiu, J. Liu, X. Wang, C. He, H. Wei, X. Yan and Z. Guo, *Nano Energy*, 2014.

27. Y. Sun, X. Hu, W. Luo and Y. Huang, *Journal of Materials Chemistry*, 2012, 22, 19190-19195.
28. J. Guo, Q. Liu, C. Wang and M. R. Zachariah, *Advanced Functional Materials*, 2012, 22, 803-811.
29. C. Zhu, A. Nobuta, Y.-W. Ju, T. Ishihara and T. Akiyama, *International Journal of Hydrogen Energy*, 2013, 38, 13419-13426.
30. C. Zhu, A. Nobuta, I. Nakatsugawa and T. Akiyama, *International Journal of Hydrogen Energy*, 2013, 38, 13238-13248.
31. C. Zhu, A. Nobuta, G. Saito, I. Nakatsugawa and T. Akiyama, *Advanced Powder Technology*, 2014, 25, 342-347.
32. C. Zhu and T. Akiyama, *Electrochimica Acta*, 2014, 127, 290-298.
33. C. Zhu and T. Akiyama, *RSC Advances*, 2014, 4, 10151-10156.
34. Z.-Y. Tian, P. Mountapmbeme Kouotou, N. Bahlawane and P. H. Tchoua Ngamou, *The Journal of Physical Chemistry C*, 2013, 117, 6218-6224.
35. N. Mironova-Ulmane, A. Kuzmin and M. Grube, *Journal of Alloys and Compounds*, 2009, 480, 97-99.
36. C. Yang, Q. Gao, W. Tian, Y. Tan, T. Zhang, K. Yang and L. Zhu, *Journal of Materials Chemistry A*, 2014, 2, 19975-19982.
37. X. Li, Y. Zhu, X. Zhang, J. Liang and Y. Qian, *RSC Advances*, 2013, 3, 10001-10006.
38. X. Gu, J. Yue, L. Chen, S. Liu, H. Xu, J. Yang, Y. Qian and X. Zhao, *Journal of Materials Chemistry A*, 2015, 3, 1037-1041.
39. T. Qiu, J. Wang, Y. Lu and W. Yang, *RSC Advances*, 2014, 4, 23027-23035.
40. Y. Xiao, X. Wang, W. Wang, D. Zhao and M. Cao, *ACS Applied Materials & Interfaces*, 2014, 6, 2051-2058.

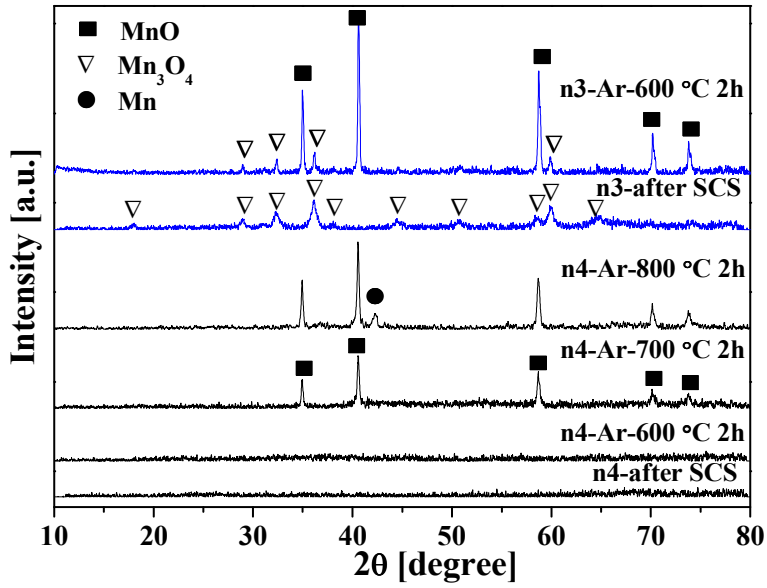

Figure 1. XRD patterns of the samples obtained at different treatment stages.

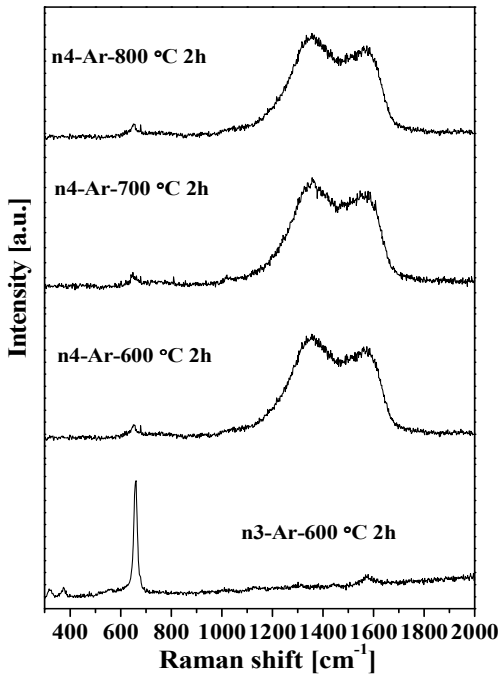

Figure 2. Raman spectra of the calcined products.

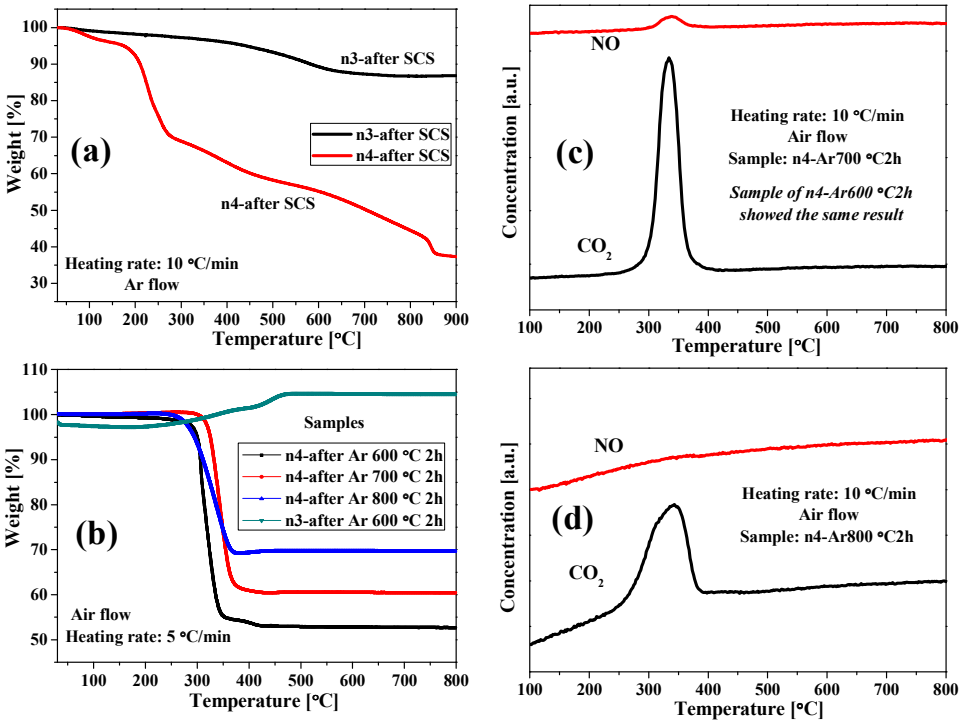

Figure 3. TG and MS analysis. (a) TG analysis of the SCSed precursors under Ar flow, (b) TG analysis of the final products under air flow to determine the carbon content, (c, d) MS spectra of NO and CO_2 gases.

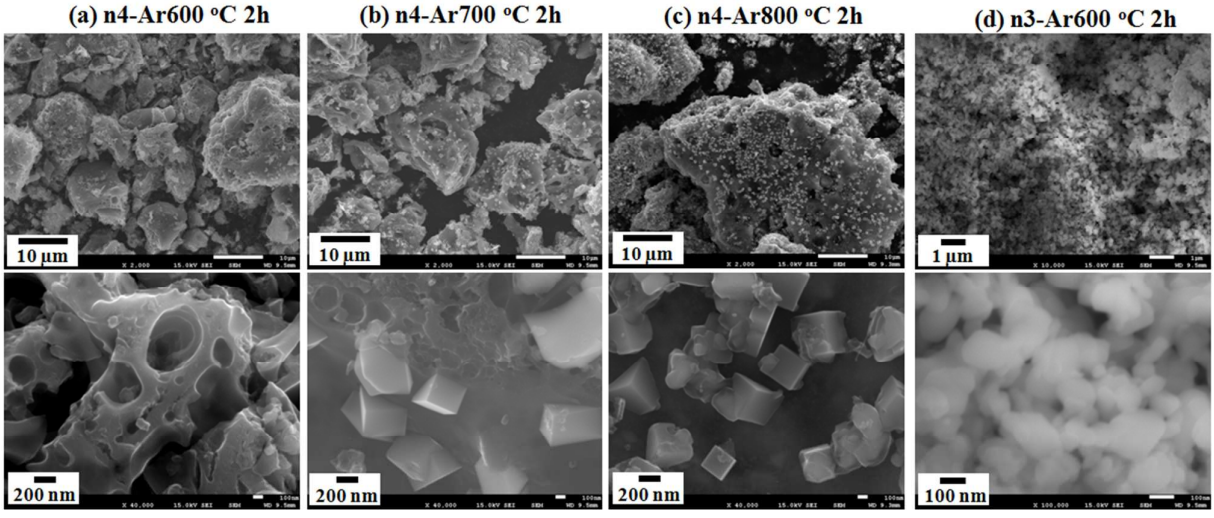

Figure 4. SEM images at different magnifications of the obtained products.

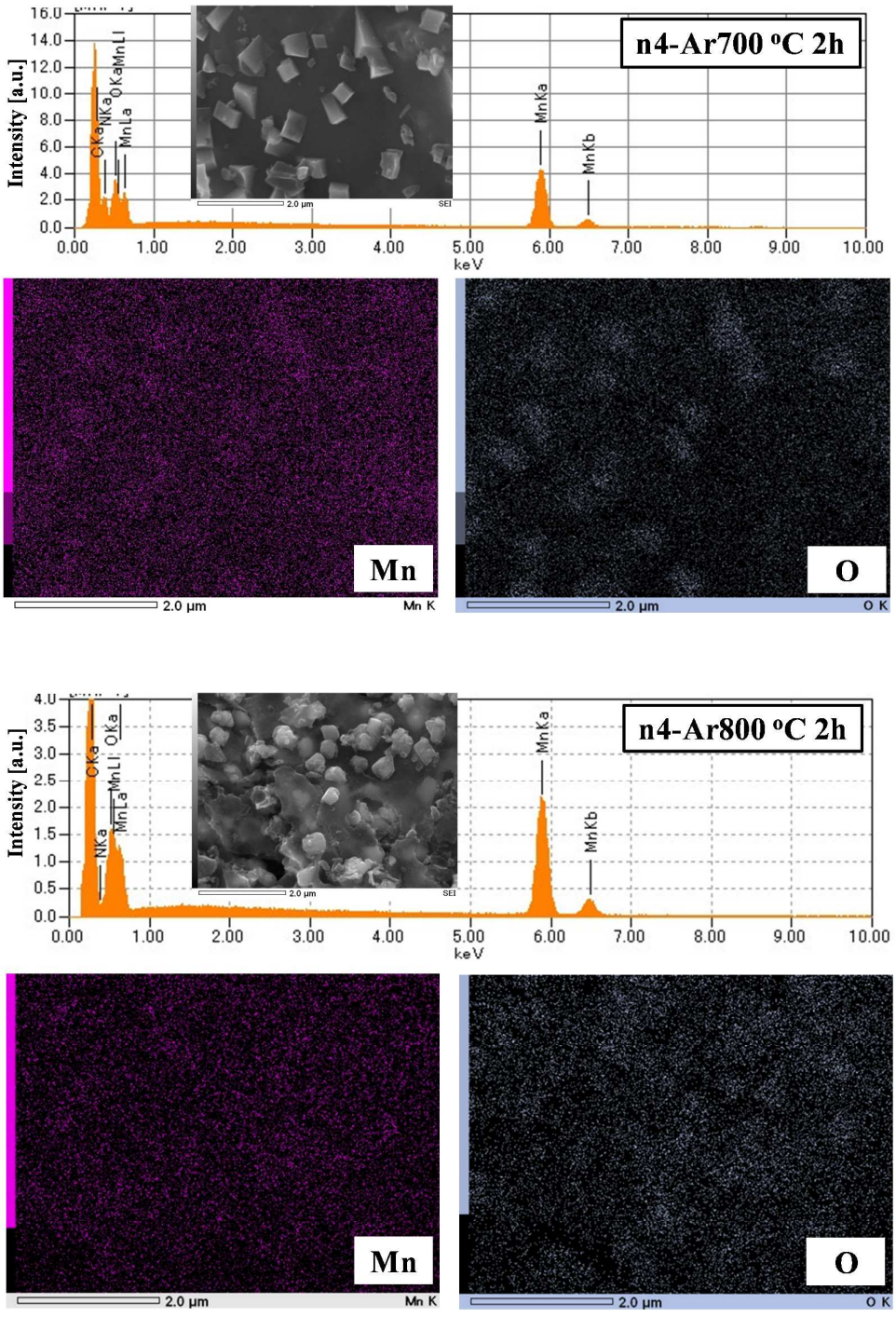

Figure 5. EDS spectra of the MnO/C composites (n4-Ar700 °C 2h and n4-Ar800 °C 2h) and the element mapping images for Mn and O. Inset SEM images show the selected analyzed area.

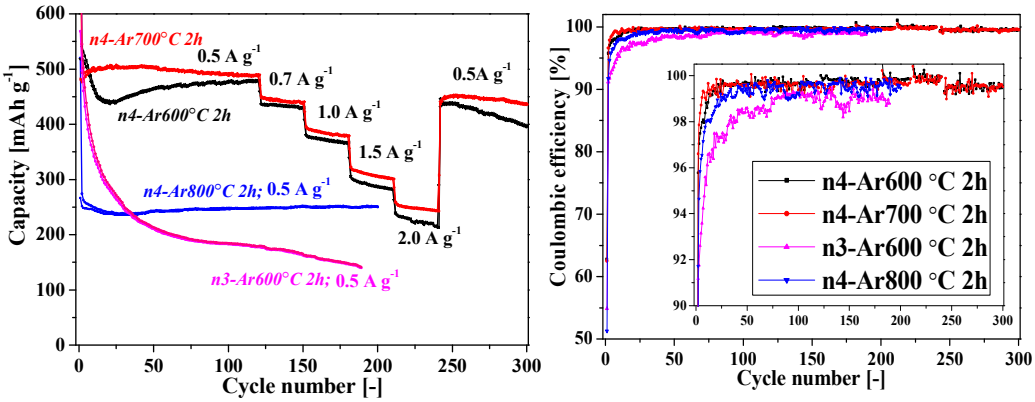

Figure 6. Cycling performance of the obtained electrodes and the related coulombic efficiency.

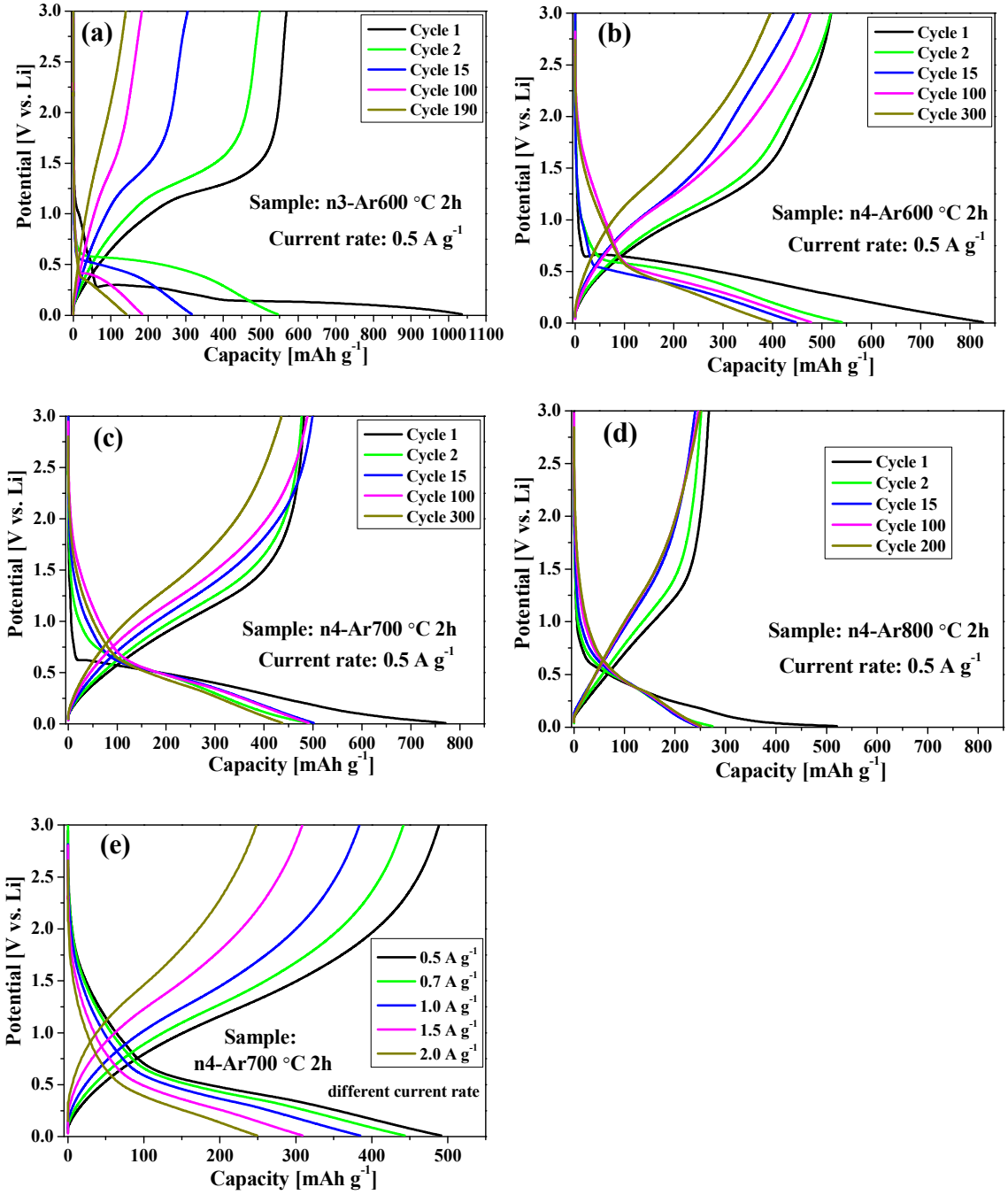

Figure 7. Discharge-charge curves of the samples at different cycles or at different current rates.

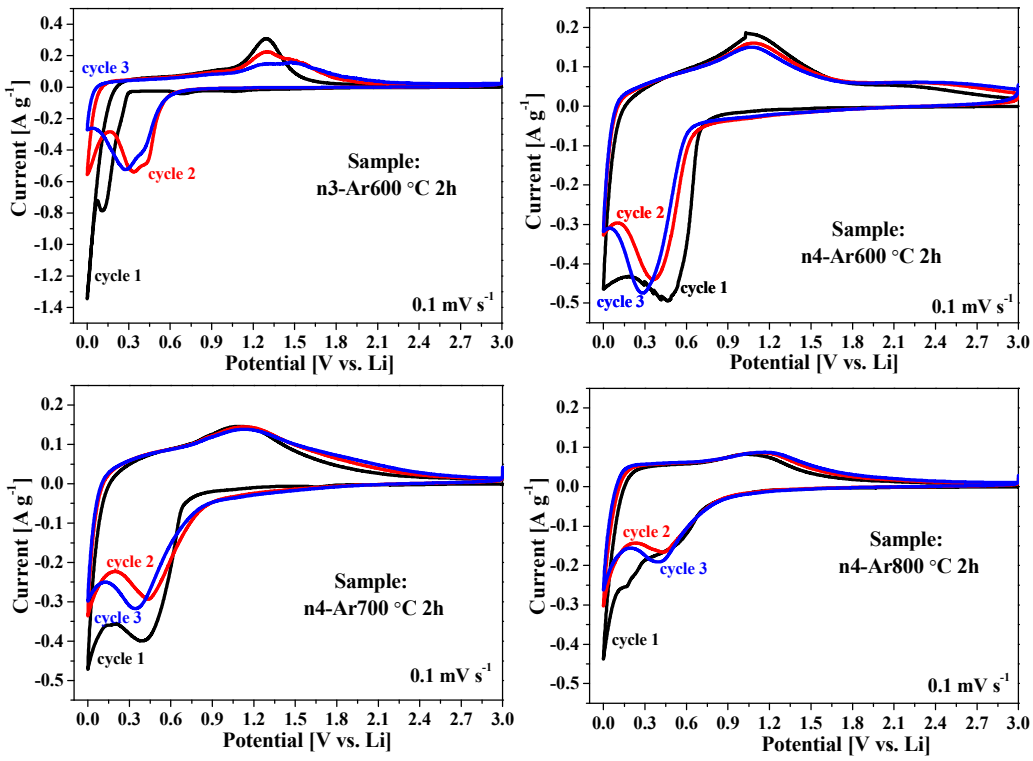

Figure 8. CV curves of the MnO/C composites during the first three cycles.